Shadow cast by a rotating black hole with anisotropic matter

Bum-Hoon Lee,[1,2,*] Wonwoo Lee,[1,†] and Yun Soo Myung[3,‡]
[1]*Center for Quantum Spacetime, Sogang University, Seoul 04107, Korea*
[2]*Department of Physics, Sogang University, Seoul 04107, Korea*
[3]*Institute of Basic Sciences and Department of Computer Simulation, Inje University, Gimhae 50834, Korea*

(Received 18 January 2021; accepted 16 February 2021; published 16 March 2021)

We obtain the shadow cast induced by the rotating black hole with an anisotropic matter. A Killing tensor representing the hidden symmetry is derived explicitly. The existence of a separability structure implies complete integrability of the geodesic motion. We analyze an effective potential around the unstable circular photon orbits to show that one side of the black hole is brighter than the other side. Further, it is shown that the inclusion of the anisotropic matter ($Kr^{2(1-w)}$) has an effect on the observables of the shadow cast. The shadow observables include approximate shadow radius R_s, distortion parameter δ_s, area of the shadow A_s, and oblateness D_{os}.

DOI: 10.1103/PhysRevD.103.064026

I. INTRODUCTION

It is interesting to note that a black hole is one of the fascinating and mystical objects in the universe. Its physical meaning and existence as a real object have developed over the past century [1–8]. It is fair to say that black holes do not seem to be directly observed. Therefore, they have been proved by indirect observations like the deflection of light rays due to the spacetime curvature [9–12], or the gravitational wave by coming from the mergers of compact binary sources [13,14].

Interestingly, the black hole has recently gained the most attention thanks to the observational reports on the shadow cast induced by the supermassive black hole [15–17] at the center of the M87 galaxy obtained by the Event Horizon Telescope collaboration [18–20]. The shadow image indicates the bright ring surrounding a dark region in the celestial sphere. The dark area describing the black hole shadow has the boundary between capture orbits and scattering orbits by photons in which photons are coming from both the accreting disc and the light source located behind a black hole, and they reach a distant observer [21–28].

Let us propose an astrophysical black hole residing in the background of matters. In this case, it is appropriate to consider a realistic black hole surrounded by a matter field or dark matter. It is well-known that dark matter [29–32] makes up about 27% of the universe and more than 90% of the matter in the Milky Way. To model a black hole in the galaxy, it is reasonable to consider the black hole coexisting with matter field or dark matter [33–35].

Analyzing the geodesic motion of a photon outside the black hole horizon is an important matter when studying astrophysical objects exposed to observations. Theoretically, studying the geodesic motion of a photon may provide a clear picture of geometrical properties for the neighborhood of a rotating black hole [36]. One may construct astrophysical models exposed to observations by describing the geodesic motion [21]. Actually, the black hole shadow could be investigated by analyzing the null geodesics around the rotating black hole.

The black hole shadow could be used to measure physical parameters (mass, charge, angular momentum, inclination angle, structure of the accretion disk). All parameters may include the effects of the black hole surrounded with matter fields or those in modified gravity theories. For this reason, the shadow cast has been extensively investigated in gravity theory with/without matter fields [21,23,37–56], other rotating objects [57–60], and modified gravity theories [61–74].

Recently, two of us have obtained the rotating black hole solution with an anisotropic matter [35] where the anisotropic matter with parameters w and K may describe both an extra U(1) field [62,75–78] and diverse dark matters. It is shown that this black hole geometry can affect the shadow when comparing with Kerr and Kerr-Newman black holes [51]. We are also interested in studying the shadow cast induced by the black hole with an anisotropic matter as a subsequent study. For this purpose, we will derive the Killing tensor and find the separability structure to guarantee the integrability of the geodesic motions. Also, we investigate an effective

*bhl@sogang.ac.kr
†warrior@sogang.ac.kr
‡ysmyung@inje.ac.kr

potential for unstable circular photon orbits to show that one side of the black hole is brighter than the other side. As additional shadow observables, we analyze the approximate shadow radius and distortion parameter. We hope that all may have a complementary relationship with one another, to describe the nature.

In this work, we wish to focus on studying the shadow cast induced by the black hole with an anisotropic matter. The paper is organized as follows. In Sec. II, we explore the symmetry of the rotating black hole geometry [79]. A Killing tensor representing the hidden symmetry is constructed and the separability structure exists. In Sec. III, we derive the geodesic equation by adopting the Hamilton-Jacobi formalism. To get the information on the boundary of the shadow cast, we study the radial null geodesic motion by making use of the effective potential. In Sec. IV, we employ a backward ray-tracing algorithm [80–82] to analyze the shadow cast induced by a rotating black hole with an anisotropic matter field described by two parameters w and K. We present the apparent shape of shadow and observables characterizing the shadow. We observe that the anisotropic matter field with w influences on the observables. Finally, we summarize our results and discuss on relevant matters in Sec. V.

II. SYMMETRY AND SEPARABILITY STRUCTURE

First of all, we consider the action

$$I=\int d^4x\sqrt{-g}\left[\frac{1}{16\pi}(R-F_{\mu\nu}F^{\mu\nu})+\mathcal{L}_{\rm am}\right]+I_b, \quad (1)$$

where $\mathcal{L}_{\rm am}$ describes effective anisotropic matter fields and I_b is the boundary term [83,84]. The rotating black hole solution with an anisotropic matter is obtained by applying the Newman-Janis algorithm to a static spherically symmetric solution as [35]

$$\begin{aligned}ds^2=&-F(r,\theta)dt^2-2[1-F(r,\theta)]a\sin^2\theta dtd\phi\\&+\frac{\Sigma}{\rho^2}\sin^2\theta d\phi^2+\frac{\rho^2}{\triangle}dr^2+\rho^2d\theta^2,\end{aligned} \quad (2)$$

where

$$\begin{aligned}F(r,\theta)&=1-\frac{2Mr-Q^2+Kr^{2(1-w)}}{\rho^2},\\ a&=\frac{J}{M},\qquad \rho^2=r^2+a^2\cos^2\theta,\\ \triangle&=r^2+a^2+Q^2-2Mr-Kr^{2(1-w)},\\ \Sigma&=\rho^2(r^2+a^2)+(2Mr-Q^2+Kr^{2(1-w)})a^2\sin^2\theta.\end{aligned} \quad (3)$$

It is important to point out that the parameters K and w control the density and anisotropy of the fluid matter surrounding the black hole. The $K=0$ case leads to the Kerr-Newman black hole and $K=0$ with $Q=0$ corresponds to the Kerr black hole, regarding as two reference black holes. This includes the rotating version of the Reissner-Nordström black hole with the constant scalar hair [77] characterized by $K<0$, $w=1$, and $a=0$. The metric is asymptotically flat for $w>0$ only. For $0\le w\le 1/2$, the energy density is not localized sufficiently such that the total energy diverges [35]. Thus, we consider the case with $w>1/2$ to obtain the geometry including a finite total energy with asymptotically flat spacetime. We allow K to take either sign for representing diverse matters surrounding the rotating black hole.

At this stage, we mention that the event (outer) horizon (r_H) for the spacetime (2) is located at the largest radius as a solution to $\triangle=0$, leading to the event horizon for Kerr-Newman black hole with $K=0$.

We are interested particularly in the ergosphere for later use in Sec. III. The ergosphere is defined as a region between surface of static limit (infinite redshift) and outer horizon [85]. On the surface, the timelike Killing vector becomes null-like as $g_{tt}=0$. Let us consider a photon emitted in the ϕ direction at radius r without r and θ momentum components. From the condition of the null trajectory, one obtains two angular velocities

$$\omega_\pm=\frac{-g_{t\phi}\pm\sqrt{\triangle\sin^2\theta}}{g_{\phi\phi}}, \quad (4)$$

where $\triangle\sin^2\theta=g_{t\phi}^2-g_{tt}g_{\phi\phi}$. Outside the event horizon ($\triangle>0$), two roots $\omega_\pm$ are alive, while there are no real roots inside the horizon. At the static limit surface satisfying $g_{tt}=0$ and $g_{t\phi}<0$, one finds $\omega_+=-\frac{2g_{t\phi}}{g_{\phi\phi}}$ and $\omega_-=0$. Inside the ergosphere ($g_{tt}>0$), one has $\omega_->0$. Therefore, all particles are necessarily corotating with the rotating black hole. On the event horizon, the two angular velocities appear the same as $\omega_\pm=\Omega|_{r=r_H}=\frac{a}{r_H^2+a^2}$.

Now, we examine the symmetry and separability structure of the rotating black hole geometry. There are explicit and hidden symmetries related to Killing vectors and Killing tensors, respectively [79,86]. Killing vectors correspond to the generators of isometries for spacetime geometry. The geometry of (2) implying a stationary axisymmetry, admits two commuting Killing vectors $\xi^\mu_{(t)}=\delta^\mu_t$ and $\xi^\mu_{(\phi)}=\delta^\mu_\phi$ [87]. On the other hand, Killing tensors correspond to a symmetric generalization of Killing vectors. A hidden symmetry represents the geometric structure of spacetime encoded in Killing tensors. This implies that an additional integral of the motion is quadratic in momentum as $\mathcal{K}^{\mu\nu}p_\mu p_\nu$ [88]. It is known that one of the Killing tensors is the metric tensor, having the structure of $g^{\mu\nu}p_\mu p_\nu=-m^2$.

We consider the null tetrad [89,90] to construct the Killing tensor. The null tetrad consists of two real null

vectors l^μ and n^μ and two complex null vectors m^μ and $\bar{m}^\mu$. They satisfy $l^\mu n_\mu = -1$, $m^\mu \bar{m}_\mu = 1$, and $l^\mu m_\mu = l^\mu \bar{m}_\mu = n^\mu m_\mu = n^\mu \bar{m}_\mu = 0$. For our purpose, we introduce an inverse metric for (2)

$$g^{\mu\nu} = \begin{pmatrix} -\frac{\Sigma}{\triangle\rho^2} & 0 & 0 & -\frac{a(1-F)}{\triangle} \\ 0 & \frac{\triangle}{\rho^2} & 0 & 0 \\ 0 & 0 & \frac{1}{\rho^2} & 0 \\ -\frac{a(1-F)}{\triangle} & 0 & 0 & \frac{\triangle - a^2\sin^2\theta}{\triangle\rho^2\sin^2\theta} \end{pmatrix}.$$

Then, $g^{\mu\nu}$ can be expressed in terms of the null tetrad as

$$g^{\mu\nu} = -l^\mu n^\nu - n^\mu l^\nu + m^\mu \bar{m}^\nu + \bar{m}^\mu m^\nu, \tag{5}$$

where the null vectors are given by

$$\begin{aligned} l^\mu &= \frac{1}{\triangle}[(r^2+a^2)\delta^\mu_0 + \triangle\delta^\mu_1 + a\delta^\mu_3], \\ n^\mu &= \frac{1}{2\rho^2}[(r^2+a^2)\delta^\mu_0 - \triangle\delta^\mu_1 + a\delta^\mu_3], \\ m^\mu &= \frac{1}{\sqrt{2}(r+ia\cos\theta)}\left[ia\sin\theta\delta^\mu_0 + \delta^\mu_2 + \frac{i}{\sin\theta}\delta^\mu_3\right], \\ \bar{m}^\mu &= \frac{1}{\sqrt{2}(r-ia\cos\theta)}\left[-ia\sin\theta\delta^\mu_0 + \delta^\mu_2 - \frac{i}{\sin\theta}\delta^\mu_3\right]. \end{aligned} \tag{6}$$

Importantly, a quadratic Killing tensor is constructed by making use of these null vectors [88,91]

$$\begin{aligned} \mathcal{K}^{\mu\nu} &= 2\rho^2 m^{(\mu}\bar{m}^{\nu)} - a^2\cos^2\theta g^{\mu\nu} \\ &= a^2\sin^2\theta\delta^\mu_0\delta^\nu_0 + 2a\delta^{(\mu}_0\delta^{\nu)}_3 + \frac{\delta^\mu_3\delta^\nu_3}{\sin^2\theta} \\ &\quad + \delta^\mu_2\delta^\nu_2 - a^2\cos^2\theta g^{\mu\nu}, \end{aligned} \tag{7}$$

which satisfies $\nabla^{(\alpha}\mathcal{K}^{\mu\nu)} = 0$ and $\mathcal{K}^{\mu\nu} = \mathcal{K}^{(\mu\nu)}$.

Let us consider the separability structure [92,93] which describes the separation of variables in the Hamilton-Jacobi formalism. We are aware that there exist two Killing vectors ($\xi^\mu_{(t)}$ and $\xi^\mu_{(\phi)}$) satisfying $\nabla^{(\alpha}\xi^{\mu)} = 0$, and two Killing tensors ($\mathcal{K}^{\mu\nu}$ and $g^{\mu\nu}$). The metric tensor also satisfies $\nabla^{(\alpha}g^{\mu\nu)} = 0$ and $g^{\mu\nu} = g^{(\mu\nu)}$. One can show that two Killing tensors mutually commute under the Schouten-Nijenhuis bracket

$$[\mathcal{K}^{\mu\nu}, g^{\mu\nu}]_{\rm SN} = 2\mathcal{K}^{\alpha(\mu}\nabla_\alpha g^{\nu\beta)} - 2g^{\alpha(\mu}\nabla_\alpha\mathcal{K}^{\nu\beta)} = 0, \tag{8}$$

which is regarded as an alternative form of the Killing tensor equation. Also, the Killing tensors and vectors satisfy

$$\begin{aligned} [\xi^\mu_{(t)}, \mathcal{K}^{\mu\nu}]_{\rm SN} &= \mathcal{L}_{\xi^\mu_{(t)}}\mathcal{K}^{\mu\nu} = [\xi^\mu_{(\phi)}, \mathcal{K}^{\mu\nu}]_{\rm SN} = [\xi^\mu_{(t)}, g^{\mu\nu}]_{\rm SN} \\ &= [\xi^\mu_{(\phi)}, g^{\mu\nu}]_{\rm SN} = [\xi^\mu_{(t)}, \xi^\mu_{(\phi)}]_{\rm SN} = 0. \end{aligned} \tag{9}$$

Therefore, we prove that the rotating black hole geometry admits the separability structure. Its existence guarantees a complete integrability of the geodesic motions.

III. GEODESIC MOTIONS

In this section, we investigate the geodesic motions [94–97]. For the static spherically symmetric black hole, one can construct four integrals of geodesic motion: test particle's energy, projection of angular momentum to an arbitrary axis, square of total angular momentum, and normalization of the four-velocity. These are conserved along the geodesics. Therefore, the geodesic equation becomes completely separable. For an axisymmetric rotating black hole, the total angular momentum is not conserved. However, determining the orbit of a test particle is a necessary step to find four integrals of the geodesic motion. In this direction, Carter has obtained the fourth constant by performing the separation of variables in the Hamilton-Jacobi formalism [98]. Here, we wish to construct four independent integrals of the geodesic motion by making use of two Killing vectors and two Killing tensors.

The four integrals of the motion are given by two conserved quantities related to Killing vectors

$$\begin{aligned} \xi^\mu_{(t)}p_\mu &= -E = -F(r,\theta)\dot{t} - [1-F(r,\theta)]a\sin^2\theta\dot{\phi}, \\ \xi^\mu_{(\phi)}p_\mu &= L_z = -[1-F(r,\theta)]a\sin^2\theta\dot{t} + \frac{\Sigma\sin^2\theta}{\rho^2}\dot{\phi}, \end{aligned} \tag{10}$$

and two conserved quantities related to Killing tensors

$$\begin{aligned} g^{\mu\nu}p_\mu p_\nu &= -m^2, \\ \mathcal{K} \equiv \mathcal{K}^{\mu\nu}p_\mu p_\nu &= p^2_\theta + (L_z - aE\sin^2\theta)^2/\sin^2\theta \\ &\quad + a^2m^2\cos^2\theta. \end{aligned} \tag{11}$$

Here, we investigate the geodesic motion around the rotating black hole by following the procedure of the separation of variables in the Hamilton-Jacobi formalism [98]. In this case, Carter's fourth constant of the motion is given by

$$\mathcal{Q} = p^2_\theta + \cos^2\theta[a^2(m^2 - E^2) + L^2_z/\sin^2\theta], \tag{12}$$

which represents the separation constant for the r and θ-directions of null geodesics. The constant of the motion is given by

$$\begin{aligned} \mathcal{Q} + (L_z - aE)^2 &= p^2_\theta + (L_z - aE\sin^2\theta)^2/\sin^2\theta \\ &\quad + a^2m^2\cos^2\theta, \end{aligned} \tag{13}$$

indicating that $\mathcal{Q}$ may be negative but $\mathcal{K}$ is always nonnegative. Equation (13) has the same form as Eq. (11) implying $\mathcal{K} \equiv \mathcal{Q} + (L_z - aE)^2$.

We notice that the geodesic motion of a neutral particle is described by the Hamilton-Jacobi equation. The geodesic equations as four first-order differential equations are found to be

$$\rho^2 p^t \equiv \rho^2 \frac{dt}{d\lambda} = -a(aE\sin^2\theta - L_z) + \frac{(r^2+a^2)P(r)}{\triangle}, \tag{14}$$

$$\rho^2 p^\phi \equiv \rho^2 \frac{d\phi}{d\lambda} = -\left(aE - \frac{L_z}{\sin^2\theta}\right) + \frac{aP(r)}{\triangle}, \tag{15}$$

$$\rho^2 p^r \equiv \rho^2 \frac{dr}{d\lambda} = \pm\sqrt{R(r)} = \triangle p_r, \tag{16}$$

$$\rho^2 p^\theta \equiv \rho^2 \frac{d\theta}{d\lambda} = \pm\sqrt{\Theta(\theta)}. \tag{17}$$

Here $+(-)$ in Eqs. (16) and (17) correspond to the outgoing (ingoing) geodesics and

$$\Theta(\theta) = \mathcal{Q} - \cos^2\theta[a^2(m^2 - E^2) + L_z^2/\sin^2\theta], \tag{18}$$

$$R(r) = P^2(r) - \triangle[m^2 r^2 + (L_z - aE)^2 + \mathcal{Q}], \tag{19}$$

$$P(r) = (r^2 + a^2)E - aL_z. \tag{20}$$

The geodesic motion of a test particle is not confined in a plane, implying that two effective potentials for the radial and latitudinal motions should be examined separately.

Now we are in a position to study the null geodesic motion with $m = 0$. It is noted that the angular size of a light source is much bigger than the angular size of the black hole. They are two important null geodesic motions named as principal congruences and unstable circular orbits. We focus on unstable circular orbits and then, mention the principal congruences briefly. The radial equation for null geodesic is given by

$$\frac{1}{2}\left(\frac{dr}{d\lambda}\right)^2 + V_{\rm eff}(r) = 0, \tag{21}$$

where the effective potential in the equatorial plane is given by

$$V_{\rm eff}(r) = -\frac{((r^2+a^2)^2 - \triangle a^2)E^2 - 2aL_z(r^2+a^2-\triangle)E + (a^2-\triangle)L_z^2}{2r^4}. \tag{22}$$

Here, we note that Carter's constant of the motion $(\mathcal{Q})$ disappears. The local maximum in the effective potentials determines the radii of unstable circular photon orbits. For $K = 0$, this reduces to the Kerr-Newman potential

$$V_{\rm eff}^{\rm KN}(r) = -\frac{[r^2(r^2+a^2) + a^2(2Mr - Q^2)]E^2 - 2aL_z(2Mr - Q^2)E + (-r^2 + 2Mr - Q^2)L_z^2}{2r^4}. \tag{23}$$

For unstable circular orbits, we have to take into account $V_{\rm eff} = 0$ and $\frac{dV_{\rm eff}}{dr} = 0$. Solving these, the location of a peak is determined as

$$r_{\rm uco} = \frac{L_z - aE}{L_z + aE}\left[3M - \frac{2Q^2}{r_{\rm uco}} + K(1+w)r_{\rm uco}^{(1-2w)}\right]. \tag{24}$$

For $K = 0$, this reduces to the Kerr-Newman case. For photon circular orbits around the extremal Kerr black hole with $a = M$, one has either $r_{\rm uco-} = M$ (corotating) or $r_{\rm uco+} = 4M$ (counterrotating case).

Carter's constant determines the test particle's motion in the θ-direction [99,100]. A physically arrowed region is defined by $\Theta(\theta) \geq 0$. The orbits cross the equatorial plane repeatedly for $\mathcal{Q} > 0$, while they remain in the equatorial plane for $\mathcal{Q} = 0$. We have the condition of $\mathcal{Q} < 0$ for the principal null congruences.

We introduce the dimensionless quantities ($\bar{a} = a/M$, $\bar{Q} = Q/M$, $\bar{K} = K/M^{2w}$, $\bar{r} = r/M$). Hereafter, we will remove the bar for simplicity.

Figure 1(a) shows the effective potential for both corotating and counterrotating cases in the equatorial plane. The left concave curves correspond to the former case, while the right concave curves to the latter case. As reference curves, black curves correspond to the Kerr one with $a = 0.9$, blue dashed curves to Kerr-Newman one [101] with $Q = 0.25$. For our work, we note that red curves denote the case with $a = 0.9$, $Q = 0$ $w = 3/2$, $K = -0.13$ while cyan curves represent the case with $a = 0.9$, $Q = 0.25$, $w = 3/2$, $K = -0.13$.

Figure 1(b) shows the locations of unstable circular orbits. The black dotted (dashed) circle indicates the location of outer horizon (static limit). The red circle denotes the unstable circle orbit for the corotating case, while the blue circle represents the counter-rotating case. We note that the unstable circle orbit for the corotating case

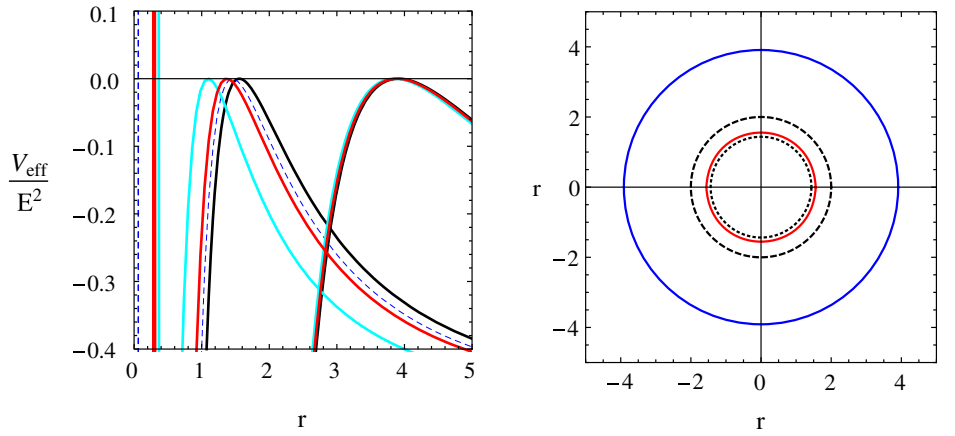

(a) Effective potentials (b) Locations of unstable circular orbits

FIG. 1. Effective potentials and locations of unstable circular orbits in the equatorial plane.

is located within the ergosphere, implying that the angular velocity of null rays for the counter-rotating case could change the sign in the ergosphere and they move along unstable circle orbit. Hence, the number of photons for corotating case is larger than those for counterrotating case when reaching the distant observer.

Now, let us consider null geodesics along $\theta = \theta_c =$ const plane. Considering that $\dot{r}$ and $\dot{\theta}$ must be real on the geodesics in Eqs. (16) and (17), one has $R(r) \geq 0$ and $\Theta(\theta) \geq 0$ in Eq. (18). $\Theta(\theta)$ is rewritten as

$$\Theta(\theta) = \mathcal{Q} + (a^2E^2 + L_z^2) - \left(a^2E^2\sin^2\theta + \frac{L_z^2}{\sin^2\theta}\right). \quad (25)$$

For $\theta = \theta_c$, one has

$$\Theta(\theta)|_{\theta=\theta_c} = 0, \qquad \partial_\theta\Theta(\theta)|_{\theta=\theta_c} = 0. \quad (26)$$

Equivalently, one finds

$$\frac{L_z}{E} = a\sin^2\theta_c, \qquad \frac{\mathcal{Q}}{E^2} = -a^2\cos^4\theta_c. \quad (27)$$

If Eq. (27) is satisfied, the solution to the geodesic equations provides the principal null geodesic. From Eqs. (14), (15), and (16) with Eq. (27), we get

$$\frac{dt}{dr} = \pm\frac{r^2 + a^2}{\triangle}, \qquad \frac{d\phi}{dr} = \pm\frac{a}{\triangle}. \quad (28)$$

The outgoing(+)/ingoing(−) congruences correspond to the two principal null congruences in Boyer-Lindquist coordinates. We may refer Refs. [102–105] for discussion on the Petrov-Pirani-Penrose classification.

For the Kerr-Newman case, (28) can be explicitly solved to give

$$\pm t = r + \frac{r_+^2 + a^2}{r_+ - r_-}\ln|r - r_+| - \frac{r_-^2 + a^2}{r_+ - r_-}\ln|r - r_-| + \text{const.} \quad (29)$$

and

$$\pm\phi = \frac{a}{r_+ - r_-}\ln\left|\frac{r - r_+}{r - r_-}\right| + \text{const.} \quad (30)$$

Finally, we mention that the ingoing principal null congruence crosses the event horizon when using Kerr (Edding-Finkelstein) coordinates.

IV. SHADOW CAST

The black hole shadow corresponds to the gravitational capture cross-section of photons. We adopt the backward ray-tracing algorithm to obtain a connection between impact parameters and celestial coordinates [82,106]. Finally, we wish to show the shadow cast induced by the rotating black hole with an anisotropic matter field.

A. Backward ray-tracing algorithm

The ray-tracing algorithm is designed for generating an image by tracing the path of light scattered off the surface of an object. There are two algorithms named forward and backward ones. The former corresponds to the method in which light rays emitted from a source are scattered off an object, enter an optical device, and finally generate the image. The latter denotes the opposite travel direction of light rays. We may trace individual light rays backward in time from an image plane.

We set up the image plane being perpendicular to the observer's line of sight to describe the black hole shadow in the celestial sphere. It is assumed that the plane (or observer) is located at an infinitely large distance from the light source with an inclination angle. The light source is

considered as both the photons passing near a black hole and emitting from an accretion disk from the observer's view.

We should choose a proper set of tetrad basis vectors $(e^{\mu}_{\hat{a}})$ to obtain the locally measured quantities by projecting photon's momentum p^{μ}. This is related to choosing the locally nonrotating frame or the reference frame of zero angular momentum observer (ZAMO) [107,108]. We note that the ZAMO frame is a local inertial frame. An observer at rest in the ZAMO frame acquires an angular velocity as an effect of frame-dragging caused by gravitational field of a rotating black hole. A useful set of the tetrad is given by

$$e^{\mu}_{\hat{t}}=\left(\frac{1}{\rho}\sqrt{\frac{\Sigma}{\triangle}},0,0,\frac{(1-F)a\rho}{\sqrt{\Sigma\triangle}}\right),\qquad e^{\mu}_{\hat{r}}=\frac{\sqrt{\triangle}}{\rho}(0,1,0,0),$$
$$e^{\mu}_{\hat{\theta}}=\frac{1}{\rho}(0,0,1,0),\qquad e^{\mu}_{\hat{\phi}}=\frac{\rho}{\sqrt{\Sigma}\sin\theta}(0,0,0,1). \tag{31}$$

Then, the locally measured energy and the momentum for photon are given by

$$p^{\hat{t}}=\frac{1}{\rho}\sqrt{\frac{\Sigma}{\triangle}}E-\frac{(1-F)a\rho}{\sqrt{\Sigma\triangle}}L_z,\qquad p^{\hat{r}}=\frac{\rho}{\sqrt{\triangle}}p^{r},$$
$$p^{\hat{\theta}}=\rho p^{\theta},\qquad p^{\hat{\phi}}=\frac{\rho}{\sqrt{\Sigma}\sin\theta}L_z, \tag{32}$$

with $p_t=-E$ and $p_\phi=L_z$. For a static observer at spatial infinity, the momentum of photon turns out to be $(w>1/2)$

$$p^{\hat{t}}\to E,\qquad p^{\hat{r}}\to p^{r},\qquad p^{\hat{\theta}}\to rp^{\theta},\qquad p^{\hat{\phi}}\to\frac{L_z}{r\sin\theta}. \tag{33}$$

B. Impact parameters

We wish to construct the Cartesian-like coordinates in the image plane to show the apparent shape of a black hole shadow composed of individual photons. Actually, these are the observation angles of α and β [82,106]. We expect that these are regarded as coordinate axes in the plane at spatial infinity. In order to get at these, we introduce two impact parameters defined as $\bar{\alpha}\equiv r_o\alpha$ and $\bar{\beta}\equiv r_o\beta$, in which r_o is computed at the position of the observer. These impact parameters correspond to the coordinate axes when taking $r_o\to\infty$. Hereafter, we will remove the bar for simplicity.

We note that $R(r)$ and $\Theta(\theta)$ must be non-negative. For the photon motion, we have

$$\frac{R(r)}{E^2}=[(r^2+a^2)-a\xi]^2-\triangle[\eta+(\xi-a)^2]\geq 0, \tag{34}$$

$$\frac{\Theta(\theta)}{E^2}=\eta+(\xi-a)^2-\left(\frac{\xi}{\sin\theta}-a\sin\theta\right)^2\geq 0, \tag{35}$$

with $\xi=L_z/E$ and $\eta=\mathcal{Q}/E^2$.

In general rotating spacetime, the unstable circular photon orbits satisfy $R|_{r=r_{\rm uco}}=0$, $R'|_{r=r_{\rm uco}}=0$, and $R''|_{r=r_{\rm uco}}>0(V''_{\rm eff}<0)$. Here the prime denotes differentiation with respect to r and $r=r_{\rm uco}$ denotes the radius for an unstable photon orbit. These conditions imply

$$[(r^2_{\rm uco}+a^2)-a\xi]^2-\triangle(r_{\rm uco})[\eta+(\xi-a)^2]=0, \tag{36}$$

$$4r_{\rm uco}[(r^2_{\rm uco}+a^2)-a\xi]-\triangle'(r_{\rm uco})[\eta+(\xi-a)^2]=0. \tag{37}$$

After eliminating η from (36) and (37) and solving for ξ, we obtain

$$\xi=\frac{r^2_{\rm uco}+a^2}{a},\qquad \xi=\frac{(r^2_{\rm uco}+a^2)\triangle'(r_{\rm uco})-4r_{\rm uco}\triangle(r_{\rm uco})}{a\triangle'(r_{\rm uco})}. \tag{38}$$

One of these is necessary for describing a black hole shadow. The first is not suitable for describing the black hole shadow because it represents principal null congruences. Taking the second solution, we solve for η from Eq. (37) to give

$$\eta=\frac{r^2_{\rm uco}[16a^2\triangle_{\rm uco}-(r_{\rm uco}\triangle'_{\rm uco}-4\triangle_{\rm uco})^2]}{a^2\triangle'^2_{\rm uco}}. \tag{39}$$

We note that ξ and η of unstable photon orbits describe the contour of a shadow. Explicitly, the unstable photon orbits are related to the boundary of a shadow. The apparent shape of a shadow is obtained by making use of the coordinates α and β lying in the celestial plane perpendicular to the line joining the observer and the center of spacetime geometry. The coordinates α and β are found to be [21,82,109]

$$\alpha=\lim_{r_o\to\infty}\left[-r_o^2\sin\theta_o\frac{d\phi}{dr}\bigg|_{(r_o,\theta_o)}\right]=-\frac{\xi}{\sin\theta_o},$$
$$\beta=\lim_{r_o\to\infty}\left[r_o^2\frac{d\theta}{dr}\bigg|_{(r_o,\theta_o)}\right]=\pm\sqrt{\eta+a^2\cos^2\theta_o-\xi^2\cot^2\theta_o}, \tag{40}$$

where (r_o,θ_o) denote the observer's position. A line joining the origin with the observer is normal to the $\alpha\beta$-plane. Approximately, it is an angular radius of shadow in two orthonormal directions. From Eq. (40), one can obtain

$$(\alpha-a\sin\theta_o)^2+\beta^2=(a+\xi)^2+\eta, \tag{41}$$

which represents the rim of the black hole reconstructed from the light rays in the unstable orbit. If $\theta_o=0$, the shadow appears spherical.

For simplicity, requiring that the observer be located in the equatorial plane $(\theta_o=\pi/2)$, α and β are directly related to ξ and η as

$$\alpha=-\xi,\qquad \beta=\pm\sqrt{\eta}. \tag{42}$$

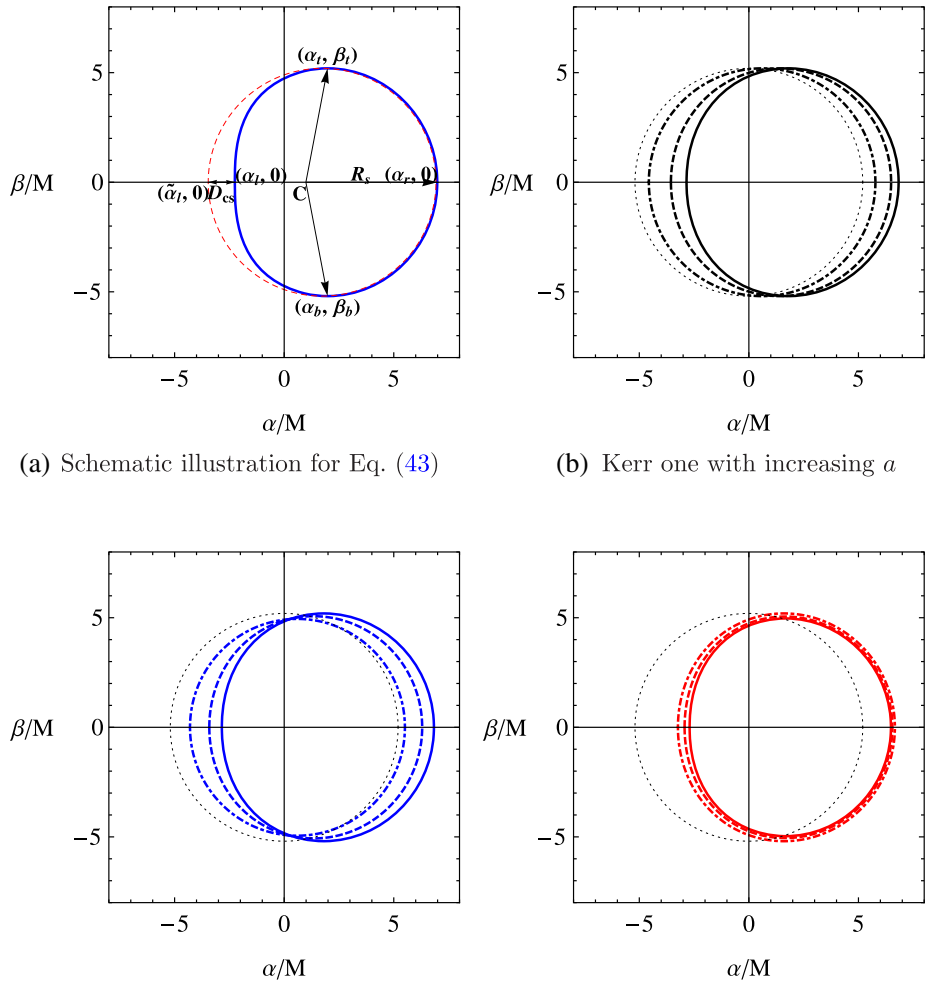

(a) Schematic illustration for Eq. (43) (b) Kerr one with increasing a

(c) Kerr one with increasing θ (d) Kerr-Newman one with increasing Q

FIG. 2. Schematic illustration for observables of a black hole shadow.

C. Shadow observables

We may use four shadow observables to extract the information on parameters of a black hole [38,42,110–112]. These include the approximate shadow radius R_s, distortion parameter δ_s, area of the shadow A_s, and oblateness D_{os}. We could determine the mass, rotation (spin), and inclination angle. Four observables take the forms

$$R_s = \frac{(\alpha_r - \alpha_t)^2 + \beta_t^2}{2|\alpha_r - \alpha_t|}, \qquad \delta_s = \frac{D_{cs}}{R_s} = \frac{|\tilde{\alpha}_l - \alpha_l|}{R_s},$$
$$A_s = 2\int_{r_{\min}}^{r_{\max}} \beta\alpha' dr, \qquad D_{os} = \frac{\alpha_r - \alpha_l}{\beta_t - \beta_b}. \tag{43}$$

Making using of *Mathematica* program based on Eqs. (40) and (43), we obtain the following figures.

Figure 2 represents schematic illustrations of a black hole shadow. The rotation direction with $a > 0$ is assumed to be counterclockwise when observing from the positive β-axis. The closed asymmetric circles represent the gravitational capture cross section of photons. The asymmetry occurs because the locations of unstable orbits for corotating and counterrotating cases are different [See Fig. 1(a)]. As we mentioned in Sec. III, the number of photons passing through the left side of the black hole rotation axis is different from that through right side. Consequently, it is found that the left side of the black hole is brighter than the right side.

In Fig. 2(a), D_{cs} denotes the difference between the left endpoints of the shadow and the reference circle. The subscript t, r, l indicate, respectively, the coordinates of the shadow vertices at the top, right, and left endpoint, while $\tilde{\alpha}_l$ is the coordinate for the left edge of referenced circle. R_s is the approximate shadow radius of the circle passing through three points, α_t, α_b, and α_r. (α_r, α_l) and (β_t, β_b) represent the horizontal and vertical diameters of the shadow, respectively.

Figure 2(b) shows the shadow of Kerr black hole with increasing a. The grey dotted circle indicates the shadow induced by Schwarzschild black hole with $a = 0$.

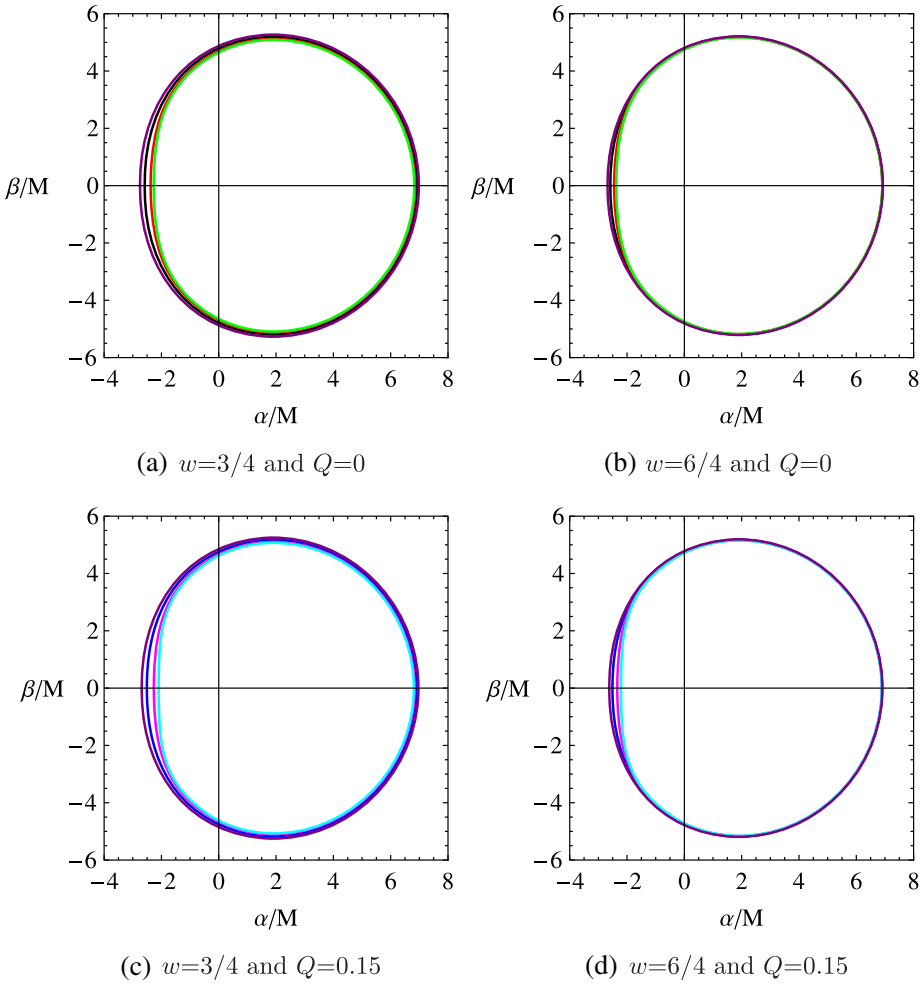

FIG. 3. Shadow casts induced by rotating black holes with anisotropic matter. (a) and (b) Kerr black hole with $Q = 0$. (c) and (d) Kerr-Newman black hole with $Q = 0.15$.

The black dot-dashed circle shows the shadow induced by Kerr black hole with $a = 0.3$, the dashed circle with $a = 0.7$, the solid circle with $a = 0.9$, respectively. The circle's vertical-axis asymmetry increases and shifts to the right as a increases.

Figure 2(c) implies the shadow of Kerr black hole with increasing θ with $a = 0.9$. The blue dot-dashed circle shows the shadow by Kerr black hole with $\theta = 17.14$, the dashed circle with $\theta = \pi/4$, the solid circle with $\theta = \pi/2$, respectively. The circle's vertical-axis asymmetry increases and shifts to the right, as θ increases.

Figure 2(d) indicates the shadow of Kerr-Newman black hole with increasing Q. The red dot-dashed circle shows the shadow induced by Kerr-Newman black hole with $a = 0.8$ and $Q = 0$ (Kerr black hole), the dashed circle with $Q = 0.4$, the solid circle with $Q = 0.5$, respectively. As Q increases, the circle's vertical-axis asymmetry increases and shifts to the right, and the area decreases.

From now on, we consider the case that the observer is located in the equatorial plane $(\theta_o = \pi/2)$.

Figure 3 represents the shadow casts by rotating black holes with selected parameters. Figure 3(a) and (b) are shadow casts with $Q = 0$, $w = 3/4$ for (a) and $w = 6/4$ for (b), while (c) and (d) are those with $Q = 0.15$, $w = 3/4$ for (c) and $w = 6/4$ for (d), respectively. In Fig. 3(a) and (b), the black circles show shadow casts by Kerr black hole, the red circles show those with $K = -0.05$, the green circles show those with $K = -0.07$, and the purple circle shows those with $K = 0.05$. In Fig. 3(c) and (d), the blue circles show shadow casts induced by Kerr-Newman black hole, the magenta circles show those with $K = -0.05$, the cyan circles show those with $K = -0.07$, and the purple circle shows those with $K = 0.05$. The circle's vertical-axis asymmetry increases and it shifts to the right, and the area increases as K increases. The difference among the deformed circles decreases as w increases. Because the positive energy condition, $Q^2 + r_o^{2w} r^{2(1-w)} \geq 0$ as shown in [35], for the cases with $K = 0.05$, we focus on figuring out the shadow cast depending on the negative K.

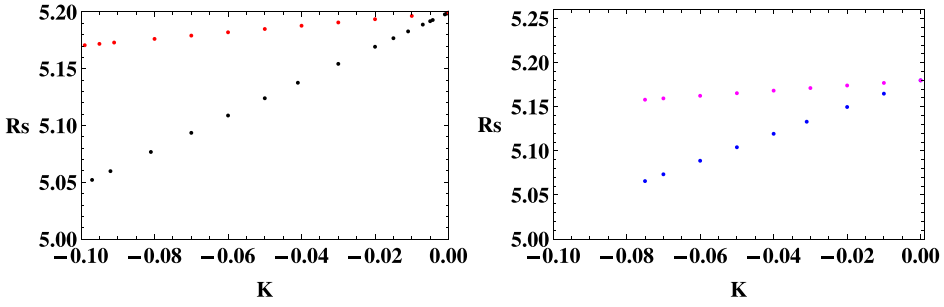

(a) Shadow radius Q=0 (b) Shadow radius Q=0.15

FIG. 4. Approximate shadow radius R_s as function of K.

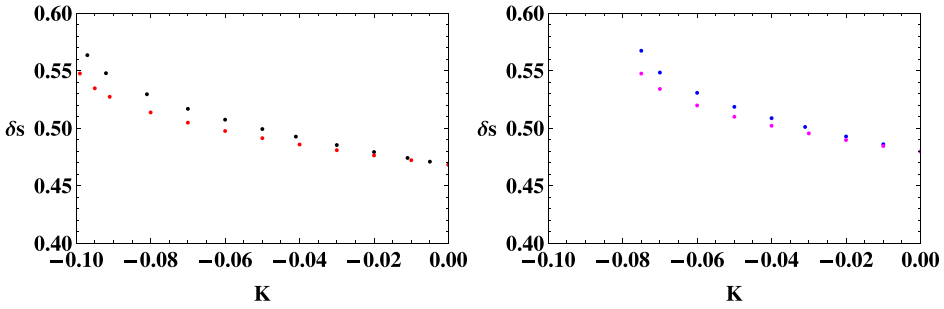

(a) Distortion parameter Q=0 (b) Distortion parameter Q=0.15

FIG. 5. Distortion parameter δ_s as function of K.

Figure 4 represents the approximate shadow radius R_s with respect to K. Figure 4(a) is the case with $a = 0.95M$ and $Q = 0$. The black dots denote the radius with $w = 3/4$, while the red dots represent the radius with $w = 6/4$. Figure 4(b) is the case with $a = 0.95M$ and $Q = 0.15M$. The blue dots correspond to the radius with $w = 3/4$, while the magenta dots correspond to the radius with $w = 6/4$. The graphs show that the approximate shadow radius R_s increases as K increases.

Figure 5 represents the distortion parameter δ_s versus K. Figure 5(a) is the case with $a = 0.95M$ and $Q = 0$. The black dots correspond to the distortion parameter with $w = 3/4$, while the red dots correspond to the distortion parameter with $w = 6/4$. Figure 5(b) is the case with $a = 0.95M$ and $Q = 0.15M$. The blue dots represent the distortion parameter with $w = 3/4$, while the magenta dots denote the distortion parameter with $w = 6/4$. These show that the distortion parameter δ_s decreases as K increases.

Figure 6 presents the area A_S with respect to K. Figure 6(a) is the case with $a = 0.95M$ and $Q = 0$. The black dots correspond to the area with $w = 3/4$, while the red dots denote the area with $w = 6/4$. Figure 6(b) is the case with $a = 0.95M$ and $Q = 0.15M$. The blue dots correspond to the area with $w = 3/4$, while the magenta

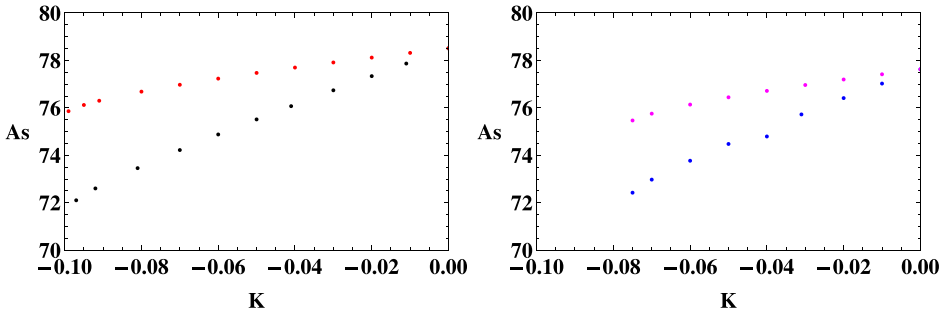

(a) Area Q=0 (b) Area Q=0.15

FIG. 6. Area A_s as function of K.

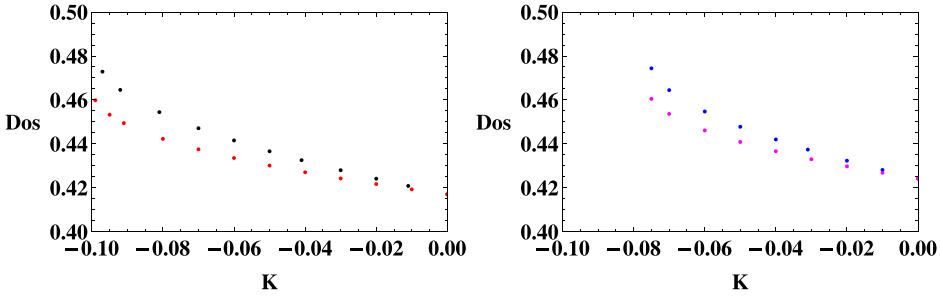

(a) Oblateness Q=0 (b) Oblateness Q=0.15

FIG. 7. Oblateness D_{os} as function of K.

dots indicate the area with $w = 6/4$. The graphs show that the area of the shadow A_s increases as K increases.

Figure 7 indicates the oblateness with respect to K. Figure 7(a) is the case with $a = 0.95M$ and $Q = 0$. The black dots correspond to the oblateness with $w = 3/4$, while the red dots correspond to the oblateness with $w = 6/4$. Figure 7(b) is the case with $a = 0.95M$ and $Q = 0.15M$. The blue dots correspond to the oblateness with $w = 3/4$, while the magenta dots correspond to the oblateness with $w = 6/4$. The graphs show that the oblateness D_{os} decreases when K increases.

V. SUMMARY AND DISCUSSIONS

We have investigated the shadow cast induced by a rotating black hole with an anisotropic matter field. For this study, we assumed that the matter field interacts with light rays through gravitational interaction. We first explored the symmetry of the rotating black hole geometry and its separability structure. We have found the Killing tensor explicitly, implying the separability structure and integrability of the geodesic motions.

The geodesic equations are derived by adopting the Hamilton-Jacobi formalism. We have analyzed the radial null geodesic motion for both corotating and counterrotating cases. The photon orbits for co-rotating cases are located inside the ergosphere, implying that some counter-rotating photons can change their rotating direction. Thus, it is found that one side of the black hole is brighter than the other side. We used the backward ray-tracing algorithm to get the relation between two impact parameters and the coordinates axes in spatial infinity. The size of the black hole shadow depends on its mass mainly, while the shape depends both rotation and inclination angle. In this work, we have taken $\theta = \pi/2$, large values of Q and K to show the difference among parameters clearly. Also, we selected specific values w. We expect that densities for Q and K are very smaller than those for mass and rotation for a real black hole.

We have presented the shadow cast induced by rotating black holes in Fig. 3. The left side corresponds to the corotating direction between the light rays and the black hole, while the right side to the counterrotating one between the light rays and the black hole. It is observed that the left side becomes flattened when K decreases. We have investigated four observables to see their dependence on parameters of a black hole. The approximate shadow radius R_s increases as K increases. The distortion parameter δ_s decreases as K increases and w has the lower value for both cases. The area of the shadow A_s increases as K increases. Lastly, the oblateness D_{os} decreases as K increases. If we require the positive energy condition satisfying $Q^2 + r_o^{2w} r^{2(1-w)} \geq 0$ as shown in [35], there will be a small room for the positive value of K. Therefore, we mainly analyzed four observables with negative values of K, except for Fig. 3 to get the deformation behavior of the shadow cast. Our results suggest that the observed black hole mass might be either underestimated or overestimated depending on the sign of the matter field (K), even though the difference is very small.

According to [18], they measured emission ring diameter $d = 42 \pm 3$ μas, angular size $11^{+0.5}_{-0.3}$ in units of mass, and observed inclination angle $\theta_o \approx 17°$ [18,113] for M87*'s shadow. It suggests that the supermassive black hole (M87*) is lying at a small angle in the direction of the observer's line of sight. Thus, the angular size seems to be similar to that for Schwarzschild black hole. However, one knows that M87* rotates with an estimated rotation $a = 0.90 \pm 0.05$ [114]. It is worth to note that a significant difference between position angles of brightness maximum measured in 2013 and 2017 was found in [115]. On the other hand, there have been attempted to make an image of SgrA* in the Milky Way [16,17,116] in the radio spectrum through very-long-baseline interferometry (VLBI) experiments [25,117]. They estimated the emission ring diameter for the source as $d \sim 50$ μas [16,17,118] and the inclination angle $\theta_o > 30°$ [119,120]. It is interesting to note that SgrA* has a larger inclination angle than M87*. Hence, one expects that its shadow cast will show an asymmetric brighter side than M87* and be detected with new-generation instruments.

Two research directions for the black hole shadow are known as theoretical and observational approaches. In this paper, we have focused on the theoretical aspect in light of

the observation. At this stage, it is not easy to determine the parameters of the rotating black hole exactly through the shadow image. However, we hope that both the upgraded EHT and the BlackHoleCam project will detect the shadow image with a much higher resolution in the near future.

Finally, we did not consider the effect of an accretion disk at all. For this, we should construct the accretion disk [121–124] in the geometry of the rotating black hole with an anisotropic matter field. This issue will be considered as an interesting subject and thus, we remain it for a future work.

ACKNOWLEDGMENTS

B.-H. L. (Grant No. NRF-2020R1F1A1075472), W. L. (Grant No. NRF-2016R1D1A1B01010234), Y. S. M. (Grant No. NRF -2017R1A2B4002057), and Center for Quantum Spacetime (CQUeST) of Sogang University (Grant No. NRF -2020R1A6A1A03047877) were supported by Basic Science Research Program through the National Research Foundation of Korea funded by the Ministry of Education. We would like to thank Gungwon Kang, Inyong Cho, Wontae Kim, and Myeong-Gu Park for helpful discussions and comments, and thank Hyeong-Chan Kim and Youngone Lee for their hospitality during our visit to Korea National University of Transportation, and Jin Young Kim to Kunsan National University. We would like to thank Yoonbai Kim and O-Kab Kwon for their hospitality at SGC 2020 held in Pohang. W. L. also would like to thank Seyen Kouwn and Hocheol Lee for helping the numerical work.

[1] K. Schwarzschild, On the gravitational field of a mass point according to Einstein's theory, Sitzungsber. Preuss. Akad. Wiss. Berlin (Math. Phys.) **1916**, 189 (1916).
[2] J. R. Oppenheimer and H. Snyder, On Continued gravitational contraction, Phys. Rev. **56**, 455 (1939).
[3] R. P. Kerr, Gravitational Field of a Spinning Mass as an Example of Algebraically Special Metrics, Phys. Rev. Lett. **11**, 237 (1963).
[4] E. T. Newman, R. Couch, K. Chinnapared, A. Exton, A. Prakash, and R. Torrence, Metric of a rotating, charged mass, J. Math. Phys. (N.Y.) **6**, 918 (1965).
[5] R. Penrose, Gravitational Collapse and Space-Time Singularities, Phys. Rev. Lett. **14**, 57 (1965).
[6] R. Penrose, Gravitational collapse: The role of general relativity, Riv. Nuovo Cimento **1**, 252 (1969); Gen. Relativ. Gravit. **34**, 1141 (2002).
[7] R. Ruffini and J. A. Wheeler, Introducing the black hole, Phys. Today **24**, No. 1, 30 (1971).
[8] A. E. Broderick, R. Narayan, J. Kormendy, E. S. Perlman, M. J. Rieke, and S. S. Doeleman, The event horizon of M87, Astrophys. J. **805**, 179 (2015).
[9] A. Einstein, Lens-like action of a star by the deviation of light in the gravitational field, Science **84**, 506 (1936).
[10] G. Reber, Cosmic static, Astrophys. J. **100**, 279 (1944).
[11] M. Schmidt, 3C 273: A Star-Like object with large redshift, Nature (London) **197**, 1040 (1963).
[12] R. Narayan and J. E. McClintock, Observational evidence for black holes, arXiv:1312.6698.
[13] B. P. Abbott *et al.* (LIGO Scientific and Virgo Collaborations), GW151226: Observation of Gravitational Waves from a 22-Solar-Mass Binary Black Hole Coalescence, Phys. Rev. Lett. **116**, 241103 (2016).
[14] B. P. Abbott *et al.* (LIGO Scientific and VIRGO Collaborations), GW170104: Observation of a 50-Solar-Mass Binary Black Hole Coalescence at Redshift 0.2, Phys. Rev. Lett. **118**, 221101 (2017); **121**, 129901(E) (2018).
[15] J. Kormendy and D. Richstone, Inward bound: The Search for supermassive black holes in galactic nuclei, Annu. Rev. Astron. Astrophys. **33**, 581 (1995).
[16] A. M. Ghez *et al.*, Measuring distance and properties of the Milky Way's central supermassive black hole with stellar orbits, Astrophys. J. **689**, 1044 (2008).
[17] S. Gillessen, F. Eisenhauer, S. Trippe, T. Alexander, R. Genzel, F. Martins, and T. Ott, Monitoring stellar orbits around the massive black hole in the galactic center, Astrophys. J. **692**, 1075 (2009).
[18] K. Akiyama *et al.* (Event Horizon Telescope Collaboration), First M87 Event Horizon Telescope results. I. The shadow of the supermassive black hole, Astrophys. J. **875**, L1 (2019).
[19] K. Akiyama *et al.* (Event Horizon Telescope Collaboration), First M87 Event Horizon Telescope results. IV. Imaging the central supermassive black hole, Astrophys. J. **875**, L4 (2019).
[20] K. Akiyama *et al.* (Event Horizon Telescope Collaboration), First M87 Event Horizon Telescope results. V. Physical origin of the asymmetric ring, Astrophys. J. **875**, L5 (2019).
[21] J. M. Bardeen, Timelike and null geodesics in the Kerr metric, in *Black Holes*, edited by C. DeWitt and B. S. DeWitt (Gordon & Breach, New York, 1973), pp. 215–239.
[22] C. T. Cunningham and J. M. Bardeen, The optical appearance of a star orbiting an extreme Kerr black hole, Astrophys. J. **183**, 237 (1973).
[23] P. J. Young, Capture of particles from plunge orbits by a black hole, Phys. Rev. D **14**, 3281 (1976).
[24] J.-P. Luminet, Image of a spherical black hole with thin accretion disk, Astron. Astrophys. **75**, 228 (1979).
[25] H. Falcke, F. Melia, and E. Agol, Viewing the shadow of the black hole at the galactic center, Astrophys. J. **528**, L13 (2000).

[26] P. V. P. Cunha and C. A. R. Herdeiro, Shadows and strong gravitational lensing: A brief review, Gen. Relativ. Gravit. **50**, 42 (2018).
[27] V. I. Dokuchaev and N. O. Nazarova, Event horizon image within black hole shadow, J. Exp. Theor. Phys. **128**, 578 (2019).
[28] R. Narayan, M. D. Johnson, and C. F. Gammie, The shadow of a spherically accreting black hole, Astrophys. J. Lett. **885**, L33 (2019).
[29] F. Zwicky, Die Rotverschiebung von extragalaktischen Nebeln, Helv. Phys. Acta **6**, 110 (1933); Gen. Relativ. Gravit. **41**, 207 (2009).
[30] V. C. Rubin and W. K. Ford, Jr., Rotation of the andromeda nebula from a spectroscopic survey of emission regions, Astrophys. J. **159**, 379 (1970).
[31] N. Aghanim *et al.* (Planck Collaboration), Planck 2018 results. VI. Cosmological parameters, Astron. Astrophys. **641**, A6 (2020).
[32] S. Kang, S. Scopel, and G. Tomar, Probing DAMA/LIBRA data in the full parameter space of WIMP effective models of inelastic scattering, Phys. Rev. D **99**, 103019 (2019).
[33] I. Cho and H. C. Kim, Simple black holes with anisotropic fluid, Chin. Phys. C **43**, 025101 (2019).
[34] I. Cho, Fluid black holes with electric field, Eur. Phys. J. C **79**, 42 (2019).
[35] H. C. Kim, B. H. Lee, W. Lee, and Y. Lee, Rotating black holes with an anisotropic matter field, Phys. Rev. D **101**, 064067 (2020).
[36] I. G. Dymnikova, Motion of particles and photons in the gravitational field of a rotating body, Sov. Phys. Usp. **29**, 215 (1986).
[37] A. de Vries, The apparent shape of a rotating charged black hole, closed photon orbits and the bifurcation set A4, Classical Quantum Gravity **17**, 123 (2000).
[38] K. Hioki and K. I. Maeda, Measurement of the Kerr spin parameter by observation of a compact object's shadow, Phys. Rev. D **80**, 024042 (2009).
[39] R. A. Konoplya, Shadow of a black hole surrounded by dark matter, Phys. Lett. B **795**, 1 (2019).
[40] F. Atamurotov, B. Ahmedov, and A. Abdujabbarov, Optical properties of black holes in the presence of a plasma: The shadow, Phys. Rev. D **92**, 084005 (2015).
[41] A. A. Abdujabbarov, L. Rezzolla, and B. J. Ahmedov, A coordinate-independent characterization of a black hole shadow, Mon. Not. R. Astron. Soc. **454**, 2423 (2015).
[42] A. Abdujabbarov, M. Amir, B. Ahmedov, and S. G. Ghosh, Shadow of rotating regular black holes, Phys. Rev. D **93**, 104004 (2016).
[43] X. Hou, Z. Xu, M. Zhou, and J. Wang, Black hole shadow of Sgr A^* in dark matter halo, J. Cosmol. Astropart. Phys. 07 (2018) 015.
[44] Z. Stuchlik, D. Charbulak, and J. Schee, Light escape cones in local reference frames of Kerr-de Sitter black hole spacetimes and related black hole shadows, Eur. Phys. J. C **78**, 180 (2018).
[45] S. Haroon, M. Jamil, K. Jusufi, K. Lin, and R. B. Mann, Shadow and deflection angle of rotating black holes in perfect fluid dark matter with a cosmological constant, Phys. Rev. D **99**, 044015 (2019).
[46] K. Jusufi, M. Jamil, P. Salucci, T. Zhu, and S. Haroon, Black hole surrounded by a dark matter halo in the M87 galactic center and its identification with shadow images, Phys. Rev. D **100**, 044012 (2019).
[47] S. W. Wei, Y. C. Zou, Y. X. Liu, and R. B. Mann, Curvature radius and Kerr black hole shadow, J. Cosmol. Astropart. Phys. 08 (2019) 030.
[48] R. Roy and U. A. Yajnik, Evolution of black hole shadow in the presence of ultralight bosons, Phys. Lett. B **803**, 135284 (2020).
[49] S. Vagnozzi, C. Bambi, and L. Visinelli, Concerns regarding the use of black hole shadows as standard rulers, Classical Quantum Gravity **37**, 087001 (2020).
[50] Z. Chang and Q. H. Zhu, Revisiting a rotating black hole shadow with astrometric observables, Phys. Rev. D **101**, 084029 (2020).
[51] J. Badia and E. F. Eiroa, Influence of an anisotropic matter field on the shadow of a rotating black hole, Phys. Rev. D **102**, 024066 (2020).
[52] V. I. Dokuchaev and N. O. Nazarova, Visible shapes of black holes M87* and SgrA*, Universe **6**, 154 (2020).
[53] P. Z. He, Q. Q. Fan, H. R. Zhang, and J. B. Deng, Shadows of rotating Hayward-de Sitter black holes with astrometric observables, Eur. Phys. J. C **80**, 1195 (2020).
[54] M. Zhang and J. Jiang, Shadows of the accelerating black holes, Phys. Rev. D **103**, 025005 (2021).
[55] A. Chowdhuri and A. Bhattacharyya, Shadow analysis for rotating black holes in the presence of plasma for an expanding universe, arXiv:2012.12914.
[56] P. Bambhaniya, D. Dey, A. B. Joshi, P. S. Joshi, D. N. Solanki, and A. Mehta, Shadows and negative precession in non-Kerr spacetime, arXiv:2101.03865.
[57] P. G. Nedkova, V. K. Tinchev, and S. S. Yazadjiev, Shadow of a rotating traversable wormhole, Phys. Rev. D **88**, 124019 (2013).
[58] C. Bambi, Can the supermassive objects at the centers of galaxies be traversable wormholes? The first test of strong gravity for mm/sub-mm very long baseline interferometry facilities, Phys. Rev. D **87**, 107501 (2013).
[59] M. Amir, K. Jusufi, A. Banerjee, and S. Hansraj, Shadow images of Kerr-like wormholes, Classical Quantum Gravity **36**, 215007 (2019).
[60] C. Bambi, K. Freese, S. Vagnozzi, and L. Visinelli, Testing the rotational nature of the supermassive object M87* from the circularity and size of its first image, Phys. Rev. D **100**, 044057 (2019).
[61] K. Hioki and U. Miyamoto, Hidden symmetries, null geodesics, and photon capture in the Sen black hole, Phys. Rev. D **78**, 044007 (2008).
[62] L. Amarilla and E. F. Eiroa, Shadow of a rotating braneworld black hole, Phys. Rev. D **85**, 064019 (2012).
[63] S. W. Wei and Y. X. Liu, Observing the shadow of Einstein-Maxwell-Dilaton-Axion black hole, J. Cosmol. Astropart. Phys. 11 (2013) 063.
[64] P. V. P. Cunha, C. A. R. Herdeiro, E. Radu, and H. F. Runarsson, Shadows of Kerr Black Holes with Scalar Hair, Phys. Rev. Lett. **115**, 211102 (2015).
[65] Z. Younsi, A. Zhidenko, L. Rezzolla, R. Konoplya, and Y. Mizuno, New method for shadow calculations:

Application to parametrized axisymmetric black holes, Phys. Rev. D **94**, 084025 (2016).
[66] M. Sharif and S. Iftikhar, Shadow of a charged rotating non-commutative black hole, Eur. Phys. J. C **76**, 630 (2016).
[67] R. Shaikh, Black hole shadow in a general rotating spacetime obtained through Newman-Janis algorithm, Phys. Rev. D **100**, 024028 (2019).
[68] S. Vagnozzi and L. Visinelli, Hunting for extra dimensions in the shadow of M87*, Phys. Rev. D **100**, 024020 (2019).
[69] A. Allahyari, M. Khodadi, S. Vagnozzi, and D. F. Mota, Magnetically charged black holes from non-linear electrodynamics and the Event Horizon Telescope, J. Cosmol. Astropart. Phys. 02 (2020) 003.
[70] R. Kumar, S. G. Ghosh, and A. Wang, Gravitational deflection of light and shadow cast by rotating Kalb-Ramond black holes, Phys. Rev. D **101**, 104001 (2020).
[71] B. Eslam Panah, K. Jafarzade, and S. H. Hendi, Charged 4D Einstein-Gauss-Bonnet-AdS Black Holes: Shadow, Energy Emission, Deflection Angle and Heat Engine, Nucl. Phys. **B961**, 115269 (2020).
[72] M. Khodadi, A. Allahyari, S. Vagnozzi, and D. F. Mota, Black holes with scalar hair in light of the Event Horizon Telescope, J. Cosmol. Astropart. Phys. 09 (2020) 026.
[73] F. Long, S. Chen, M. Wang, and J. Jing, Shadow of a disformal Kerr black hole in quadratic DHOST theories, Eur. Phys. J. C **80**, 1180 (2020).
[74] E. Contreras, A. Rincon, G. Panotopoulos, and P. Bargueno, Geodesic analysis and black hole shadows on a general non–extremal rotating black hole in five–dimensional gauged supergravity, arXiv:2010.03734.
[75] J. Schee and Z. Stuchlik, Optical phenomena in the field of braneworld Kerr black holes, Int. J. Mod. Phys. D **18**, 983 (2009).
[76] D. Astefanesei, C. Herdeiro, A. Pombo, and E. Radu, Einstein-Maxwell-scalar black holes: Classes of solutions, dyons and extremality, J. High Energy Phys. 10 (2019) 078.
[77] D. C. Zou and Y. S. Myung, Scalar hairy black holes in Einstein-Maxwell-conformally coupled scalar theory, Phys. Lett. B **803**, 135332 (2020).
[78] Y. S. Myung and D. C. Zou, Scalarized charged black holes in the Einstein-Maxwell-Scalar theory with two U(1) fields, Phys. Lett. B **811**, 135905 (2020).
[79] V. Frolov, P. Krtous, and D. Kubiznak, Black holes, hidden symmetries, and complete integrability, Living Rev. Relativity **20**, 6 (2017).
[80] F. H. Vincent, T. Paumard, E. Gourgoulhon, and G. Perrin, GYOTO: A new general relativistic ray-tracing code, Classical Quantum Gravity **28**, 225011 (2011).
[81] O. James, E. von Tunzelmann, P. Franklin, and K. S. Thorne, Gravitational lensing by spinning black holes in astrophysics, and in the movie interstellar, Classical Quantum Gravity **32**, 065001 (2015).
[82] P. V. P. Cunha, C. A. R. Herdeiro, E. Radu, and H. F. Runarsson, Shadows of Kerr black holes with and without scalar hair, Int. J. Mod. Phys. D **25**, 1641021 (2016).
[83] G. W. Gibbons and S. W. Hawking, Action integrals and partition functions in quantum gravity, Phys. Rev. D **15**, 2752 (1977).
[84] S. W. Hawking and S. F. Ross, Duality between electric and magnetic black holes, Phys. Rev. D **52**, 5865 (1995).
[85] R. Ruffini and J. A. Wheeler, Relativistic cosmology and space platforms, Report No. PRINT-70-2077.
[86] L. P. Eisenhart, *Riemannian Geometry* (Princeton University Press, Princeton, NJ, 1949).
[87] B. Carter, Axisymmetric Black Hole Has Only Two Degrees of Freedom, Phys. Rev. Lett. **26**, 331 (1971).
[88] M. Walker and R. Penrose, On quadratic first integrals of the geodesic equations for type {22} spacetimes, Commun. Math. Phys. **18**, 265 (1970).
[89] W. Kinnersley, Type D vacuum metrics, J. Math. Phys. (N.Y.) **10**, 1195 (1969).
[90] H. Kim, C. H. Lee, and H. K. Lee, Nonvanishing magnetic flux through the slightly charged Kerr black hole, Phys. Rev. D **63**, 064037 (2001).
[91] S. Chandrasekhar, *The Mathematical Theory of Black Holes* (Clarendon, Oxford, UK, 1985).
[92] S. Benenti and M. Francaviglia, Remarks on certain separability structures and their applications to general relativity, Gen. Relativ. Gravit. **10**, 79 (1979).
[93] M. Demianski and M. Francaviglia, Separability structures and Killing-Yano tensors in vacuum type-D space-times without acceleration, Int. J. Theor. **19**, 675 (1980).
[94] B. Gwak, B. H. Lee, and W. Lee, Geodesic properties and orbits in 5-dimensional hypercylindrical spacetime, J. Korean Phys. Soc. **54**, 2202 (2009).
[95] B. Gwak, B. H. Lee, W. Lee, and H. C. Kim, Geodesic motions in extraordinary string geometry, Gen. Relativ. Gravit. **43**, 2277 (2011).
[96] H. C. Lee and Y. J. Han, Innermost stable circular orbit of Kerr-MOG black hole, Eur. Phys. J. C **77**, 655 (2017).
[97] C. L. A. Rizwan, A. Naveena Kumara, K. Hegde, M. S. Ali, and A. K. M, Rotating black hole with an anisotropic matter field as a particle accelerator, arXiv:2008.01426.
[98] B. Carter, Global structure of the Kerr family of gravitational fields, Phys. Rev. **174**, 1559 (1968).
[99] D. C. Wilkins, Bound geodesics in the Kerr metric, Phys. Rev. D **5**, 814 (1972).
[100] E. Teo, Spherical photon orbits around a Kerr black hole, Gen. Relativ. Gravit. **35**, 1909 (2003).
[101] M. Zajacek, A. Tursunov, A. Eckart, and S. Britzen, On the charge of the galactic centre black hole, Mon. Not. R. Astron. Soc. **480**, 4408 (2018).
[102] A. Z. Petrov, The classification of spaces defining gravitational fields, Gen. Relativ. Gravit. **32**, 1665 (2000).
[103] F. A. E. Pirani, Invariant formulation of gravitational radiation theory, Phys. Rev. **105**, 1089 (1957).
[104] R. Penrose, A spinor approach to general relativity, Ann. Phys. (N.Y.) **10**, 171 (1960).
[105] C. W. Misner, K. S. Thorne, and J. A. Wheeler, *Gravitation* (W. H. Freeman, San Francisco, 1973).
[106] D. Psaltis and T. Johannsen, A ray-tracing algorithm for spinning compact object spacetimes with arbitrary quadrupole moments. I. Quasi-Kerr black holes, Astrophys. J. **745**, 1 (2012).

[107] J. M. Bardeen, W. H. Press, and S. A. Teukolsky, Rotating black holes: Locally nonrotating frames, energy extraction, and scalar synchrotron radiation, Astrophys. J. **178**, 347 (1972).
[108] V. P. Frolov and I. D. Novikov, *Black Hole Physics: Basic Concepts and New Developments* (Kluwer Academic Publishers, 1998).
[109] S. E. Vazquez and E. P. Esteban, Strong field gravitational lensing by a Kerr black hole, Nuovo Cimento Soc. Ital. Fis. **119B**, 489 (2004).
[110] R. Takahashi, Shapes and positions of black hole shadows in accretion disks and spin parameters of black holes, J. Korean Phys. Soc. **45**, S1808 (2004); Astrophys. J. **611**, 996 (2004).
[111] O. Y. Tsupko, Analytical calculation of black hole spin using deformation of the shadow, Phys. Rev. D **95**, 104058 (2017).
[112] R. Kumar and S. G. Ghosh, Black hole parameter estimation from its shadow, Astrophys. J. **892**, 78 (2020).
[113] R. Craig Walker, P. E. Hardee, F. B. Davies, C. Ly, and W. Junor, The structure and dynamics of the subparsec Jet in M87 based on 50 VLBA observations over 17 years at 43 GHz, Astrophys. J. **855**, 128 (2018).
[114] F. Tamburini, B. Thide, and M. Della Valle, Measurement of the spin of the M87 black hole from its observed twisted light, Mon. Not. R. Astron. Soc. **492**, L22 (2020).
[115] M. Wielgus *et al.* (Event Horizon Telescope Collaboration), Monitoring the morphology of M87* in 2009–2017 with the Event Horizon Telescope, Astrophys. J. **901**, 67 (2020).
[116] B. Balick and R. L. Brown, Intense sub-arcsecond structure in the galactic center, Astrophys. J. **194**, 265 (1974).
[117] C. Goddi *et al.*, BlackHoleCam: Fundamental physics of the galactic center, Int. J. Mod. Phys. D **26**, 1730001 (2017).
[118] R. S. Lu *et al.*, Detection of intrinsic source structure at 3 Schwarzschild radii with Millimeter-VLBI observations of SAGITTARIUS A*, Astrophys. J. **859**, 60 (2018).
[119] A. E. Broderick, V. L. Fish, S. S. Doeleman, and A. Loeb, Estimating the parameters of Sgr A*'s accretion flow Via millimeter VLBI, Astrophys. J. **697**, 45 (2009).
[120] M. J. Reid *et al.*, Trigonometric parallaxes of high mass star forming regions: The structure and kinematics of the Milky Way, Astrophys. J. **783**, 130 (2014).
[121] I. D. Novikov and K. S. Thorne, Astrophysics and black holes, in *Black Holes*, edited by C. DeWitt and B. S. DeWitt (Gordon & Breach, New York, 1973), pp. 343–550.
[122] D. N. Page and K. S. Thorne, Disk-accretion onto a black hole. Time-averaged structure of accretion disk, Astrophys. J. **191**, 499 (1974).
[123] U. Jang, Y. Yi, and H. Kim, Thick accretion disk and its super Eddington luminosity around spinning blackholes, arXiv:2002.10885.
[124] L. G. Collodel, D. D. Doneva, and S. S. Yazadjiev, Circular orbits structure and thin accretion disks around Kerr black holes with scalar hair, arXiv:2101.05073.